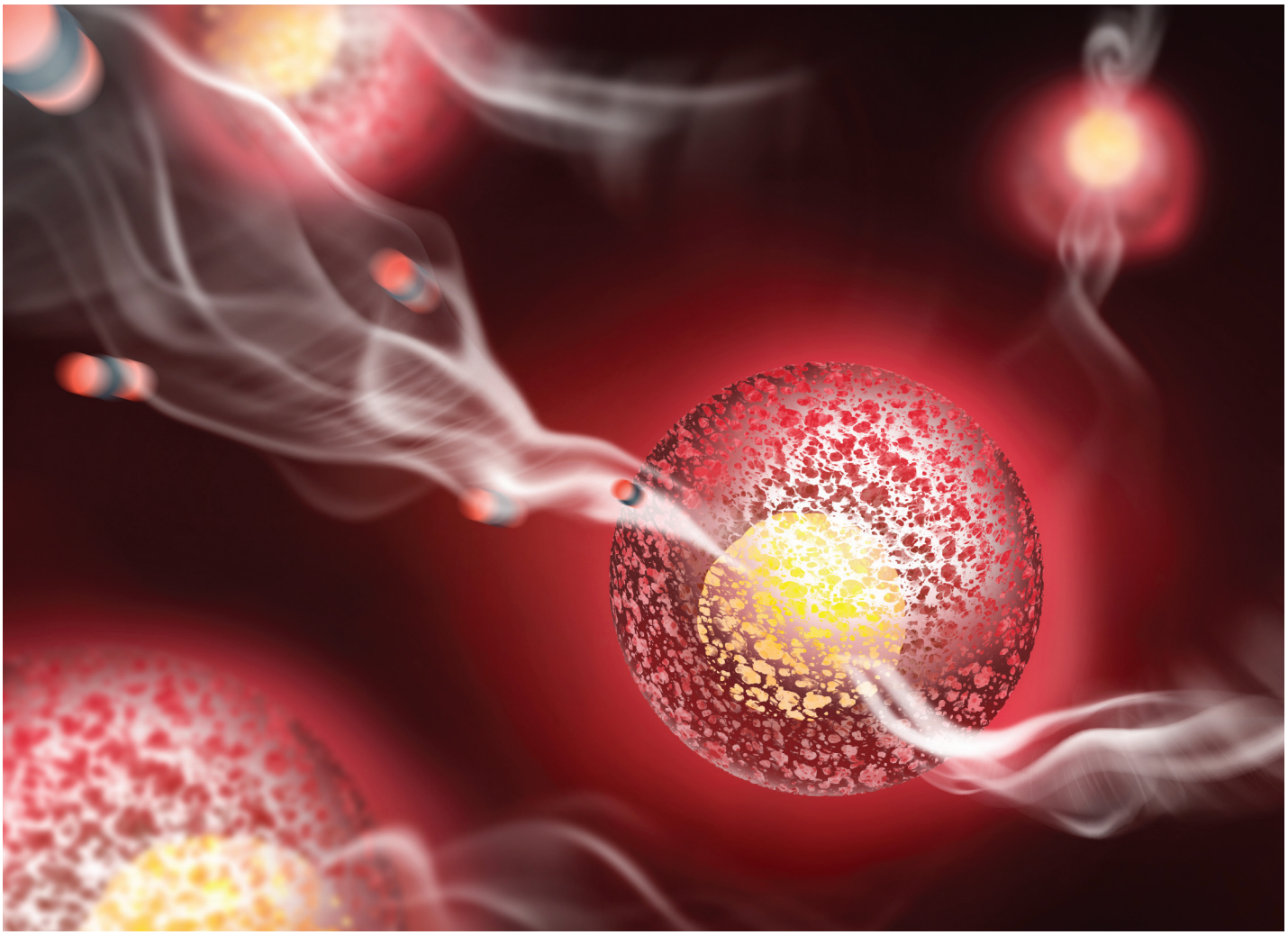

**Showcasing research from Prof. Christoph R. Müller's group at the Laboratory of Energy Science and Engineering of ETH Zürich, Zürich, Switzerland.**

Yolk–shell-type CaO-based sorbents for $CO_2$ capture: assessing the role of nanostructuring for the stabilization of the cyclic $CO_2$ uptake

Nanostructuring allows the elucidation of effective mechanisms for the stabilization of CaO-based solid sorbents for $CO_2$ capture. Combining wet-chemistry synthesis and an arsenal of characterization techniques, yolk–shell-type architectures are synthesized and studied in depth to challenge our current understanding of the engineering of CaO-based sorbents. Yolk–shell-type architectures stabilize CaO over many $CO_2$ capture and release cycles by mitigating deactivation routes such as sintering and the formation of inactive mixed oxides.

## As featured in:

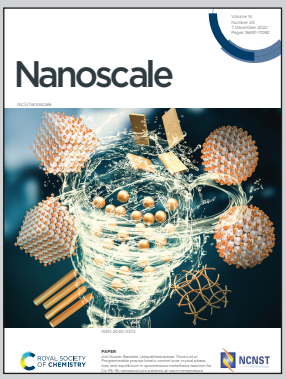


See Christoph R. Müller *et al.*, *Nanoscale*, 2022, **14**, 16816.

ROYAL SOCIETY OF CHEMISTRY

rsc.li/nanoscale

Registered charity number: 207890

Nanoscale

ROYAL SOCIETY OF CHEMISTRY

PAPER

View Article Online
View Journal | View Issue



Cite this: *Nanoscale*, 2022, **14**, 16816

# Yolk–shell-type CaO-based sorbents for $CO_2$ capture: assessing the role of nanostructuring for the stabilization of the cyclic $CO_2$ uptake†

Maximilian Krödel, Alexander Oing, Jan Negele, Annelies Landuyt, Agnieszka Kierzkowska, Alexander H. Bork, Felix Donat and Christoph R. Müller *

Improving the cyclic $CO_2$ uptake stability of CaO-based solid sorbents can provide a means to lower $CO_2$ capture costs. Here, we develop nanostructured yolk(CaO)–shell($ZrO_2$) sorbents with a high cyclic $CO_2$ uptake stability which outperform benchmark CaO nanoparticles after 20 cycles (0.17 $g_{CO_2}$ $g_{Sorbent}^{-1}$) by more than 250% (0.61 $g_{CO_2}$ $g_{Sorbent}^{-1}$), even under harsh calcination conditions (*i.e.* 80 vol% $CO_2$ at 900 °C). By comparing the yolk–shell sorbents to core–shell sorbents, *i.e.* structures with an intimate contact between the stabilizing phase and CaO, we are able to identify the main mechanisms behind the stabilization of the $CO_2$ uptake. While a yolk–shell architecture stabilizes the morphology of single CaO nanoparticles over repeated cycling and minimizes the contact between the yolk and shell materials, core–shell architectures lead to the formation of a thick $CaZrO_3$-shell around CaO particles, which limits $CO_2$ transport to unreacted CaO. Hence, yolk–shell architectures effectively delay $CaZrO_3$ formation which in turn increases the theoretically possible $CO_2$ uptake since $CaZrO_3$ is $CO_2$-capture-inert. In addition, we observe that yolk–shell architectures also improved the carbonation kinetics in both the kinetic- and diffusion-controlled regimes leading to a significantly higher cyclic $CO_2$ uptake for yolk–shell-type sorbents.

Received 16th August 2022,
Accepted 10th October 2022

DOI: 10.1039/d2nr04492g

rsc.li/nanoscale



## 1. Introduction

Climate change due to anthropogenic greenhouse gas emissions into the atmosphere is one of the most pressing challenges of our modern society.[1,2] Net greenhouse gas emissions have to be reduced significantly in order to reach the IPCC's recommendation of limiting global warming to less than 2 °C compared to pre-industrial levels.[3] Carbon dioxide capture and storage (CCS) technologies are a potential near- to mid-term solution to mitigate the emissions of carbon dioxide ($CO_2$), arguably the most prominent greenhouse gas.[3] CaO-based sorbents are a viable class of materials to capture $CO_2$ emitted by large point sources.[4–6] The associated cyclic $CO_2$ capture process is referred to as calcium looping (CaL) and is based on the reversible reaction of CaO and $CO_2$:

$$CaO(s) + CO_2(g) \leftrightarrow CaCO_3(s) \quad (\Delta H^{\circ}_{298\,K} = -179\,kJ\,mol^{-1})$$

CaO-based sorbents are non-toxic and cost-effective (estimated capture cost of <30 USD per $t_{CO_2}$) compared to the current benchmark technology for $CO_2$ capture, *i.e.* amine scrubbing (estimated capture costs of 40 to 55 USD per $t_{CO_2}$).[7–9] However, CaO-based sorbents are prone to rapid deactivation, *i.e.* a reduction of their cyclic $CO_2$ uptake capacity from a theoretical maximum of 0.78 $g_{CO_2}$ $g_{CaO}^{-1}$ to typically <0.2 $g_{CO_2}$ $g_{CaO}^{-1}$, largely due to sintering at the high operating temperatures (around 650–900 °C).[10–12] Various approaches to mitigate sintering-induced deactivation have been reported, including (I) the addition of high Tammann-temperature stabilizers such as MgO, $Al_2O_3$ or $ZrO_2$,[13–18] (II) the (re-)structuring of the morphology of sorbents,[14,19] *e.g.* using steam treatment,[20] or (III) the manufacture of materials with a high surface area and pore volume.[19]

The stabilization of CaO-based sorbents using metal oxides such as MgO, $Al_2O_3$ and $ZrO_2$ has been widely applied and currently there are very few new sorbent formulations that do not contain either such structural stabilizers, promoters (*e.g.* alkali metal salts like $Na_2CO_3$) or other performance-enhancing precursors (*e.g.* Ca-precursors containing alcohol groups).[5,14,16,17,21–25] The best reported materials exhibit cyclic $CO_2$ uptakes of up to 0.65 $g_{CO_2}$ $g_{Sorbent}^{-1}$ after 10 carbonation–

*Department of Mechanical and Process Engineering, Laboratory of Energy Science and Engineering, ETH Zurich, Leonhardstrasse 21, 8092 Zurich, Switzerland. E-mail: muelchri@ethz.ch*

† Electronic supplementary information (ESI) available. See DOI: https://doi.org/10.1039/d2nr04492g

calcination cycles, which is six times higher compared to the benchmark limestone.[26] Here, the high Tammann-temperature stabilizer MgO is believed to act as a physical barrier (spacer) between the CaO grains, reducing in turn their sintering (or the sintering of the $CaCO_3$ formed).[5,21,27,28] Hence, the size and distribution of these structural stabilizers within the CaO matrix must play an important role in mitigating sintering. It is important to note that the homogeneity of the distribution of the stabilizer might dynamically change with cycling (and indeed possibly even within one carbonation–calcination cycle). For example, Kim *et al.*[15] observed that the stabilizer $Ca_3Al_2O_6$ migrates to the surface of CaO particles during cycling, reducing in turn the stabilizer's effectiveness in reducing sintering. Therefore, one of the proposed design criteria for effective CaO-based sorbents is a low mobility of the stabilizing phase to avoid the loss of its stabilizing functionality. In addition, many investigated stabilizers form mixed phases with CaO at CaL conditions (650–900 °C) that are inactive for $CO_2$ uptake, *e.g.* $Ca_3Al_2O_3$ or $CaZrO_3$.[11,19,29,30] The formation of mixed phases that do not absorb $CO_2$ results in a reduced amount of reactive CaO, reducing the theoretically achievable $CO_2$ uptake of the sorbent. Hence, the synthesis of structures in which the interaction between CaO and the stabilizer is minimized to limit the formation of $CO_2$-capture-inactive mixed oxides is desirable.

Like many gas–solid reactions, the carbonation reaction of CaO proceeds in two principal reaction regimes: a kinetically-controlled, rapid $CO_2$ uptake regime that is followed by a much slower, diffusion-controlled $CO_2$ uptake regime.[31–33] While the $CO_2$ uptake during the kinetically-controlled regime is largely controlled by the available pore volume and surface area, the apparent rate of reaction in the diffusion-controlled reaction regime is affected by morphological and structural parameters, *e.g.* the effective diffusivity of $CO_2$ in the material.[21] In previous works, the transition between the two reaction regimes has been associated with the formation of a product layer of $CaCO_3$ on top of CaO, which causes the blockage of pores such that a certain fraction of the pore volume and surface area of the sorbent becomes inaccessible for $CO_2$ molecules.[34–36] For a two-dimensional surface of a non-porous material it has been hypothesized that once the product layer reaches a critical thickness (estimated to be around 30–50 nm by various works[34,37,38]), the reaction transitions from kinetic control to diffusion control.[39] To maximize the $CO_2$ uptake in the kinetically-controlled regime, the nanostructuring of CaO (*i.e.* particle size < 60–100 nm) is highly favorable. Previous works concerned with CaO (or $CaCO_3$) nanoparticles of size < 100 nm investigated uncoated nanoparticles or nanoparticles with coatings that have an intimate contact with the CaO nanoparticle core (core–shell structures), resulting in the formation of $CO_2$-capture-inactive mixed phases and hence comparatively low $CO_2$ uptake.[40,41] For example, core–shell structures with $CaCO_3$ cores and shells of $ZrO_2$ or $SiO_2$ have been reported to yield materials with a significantly stabilized cyclic $CO_2$ uptake compared to bare $CaCO_3$.[29,42,43] However, these materials deactivated over prolonged cyclic operation *via* the formation of mixed oxides with calcium that both reduce the amount of CaO available for reaction and also affect negatively the carbonation kinetics. Instead, the structure of an optimized model CaO-based sorbent should exhibit the following attributes: (I) the structure should be composed of CaO nanoparticles of size < 100 nm to reduce the effect of product layer diffusion limitation.[5,34,37] (II) It should utilize a stabilizer to avoid physical contact (and hence sintering) between the individual CaO nanoparticles. Applying a stabilizer shell around the CaO nanoparticles would yield this physical separation, but the direct contact between the stabilizer and CaO might lead to the formation of $CO_2$-capture-inactive mixed phases. To prevent such direct contact, a sacrificial layer can be placed between the CaO nanoparticle and the stabilizer coating, creating upon its removal a space between the CaO nanoparticle and the stabilizing coating. (III) The stabilizer shell needs to be porous to allow for a fast transport of $CO_2$ to the surface of CaO. Overall, these requirements would demand a yolk–shell-type structure. Hence in this work, we report on the synthesis of such model, yolk–shell-structured sorbents to probe whether the aforementioned requirements concerning sorbent design are indeed correct and to understand better the deactivation and stabilization mechanisms of nanostructured sorbents. We note that such sorbents are very likely not to be directly usable in an industrial $CO_2$ sorption process in which mechanical stability of sorbent particles may be one of many additional constraints. However, the insights gained from this study will help to understand better the functioning of stabilizers, aiding the design of practically applicable, yet still superior sorbent systems.

To this end, we use $CaCO_3$ nanoparticles with an average particle size < 100 nm that are stabilized by a porous shell of $ZrO_2$ in a yolk(CaO)–shell($ZrO_2$) architecture. The presence of a yolk–shell-type structure is shown to ensure a high sintering resistance and high rates of transport of $CO_2$ to CaO, while the formation of the $CO_2$-capture-inactive $CaZrO_3$ phase is avoided. The design approach is depicted in Fig. 1.

## 2. Experimental

### 2.1 Materials

**2.1.1 Synthesis of a sacrificial carbonaceous shell.** To minimize the contact area between CaO and the stabilizer, the $CaCO_3$ nanoparticles were first coated with a carbonaceous shell using a mixture of resorcinol and formaldehyde.[44] Here, 100 mg of the $CaCO_3$ nanoparticles (≥97.5%, SkySpring Nanomaterials) was dispersed in a mixture of 60 mL deionized water and 19.7 g ethanol by ultrasonicating the suspension for 30 minutes. Subsequently, 150 mg of hexadecyltrimethylammonium bromide (CTAB, ≥99%, BioXtra, Sigma Aldrich) was added and the solution was stirred for 20 minutes. Next, 32 mg of resorcinol (≥98%, Sigma Aldrich) and 45 μL of a formaldehyde solution (37–41 wt% aqueous solution, Fisher Scientific) were added to the system. After the complete dissolution of the precursors, 0.4 mL of a 25 wt% aqueous

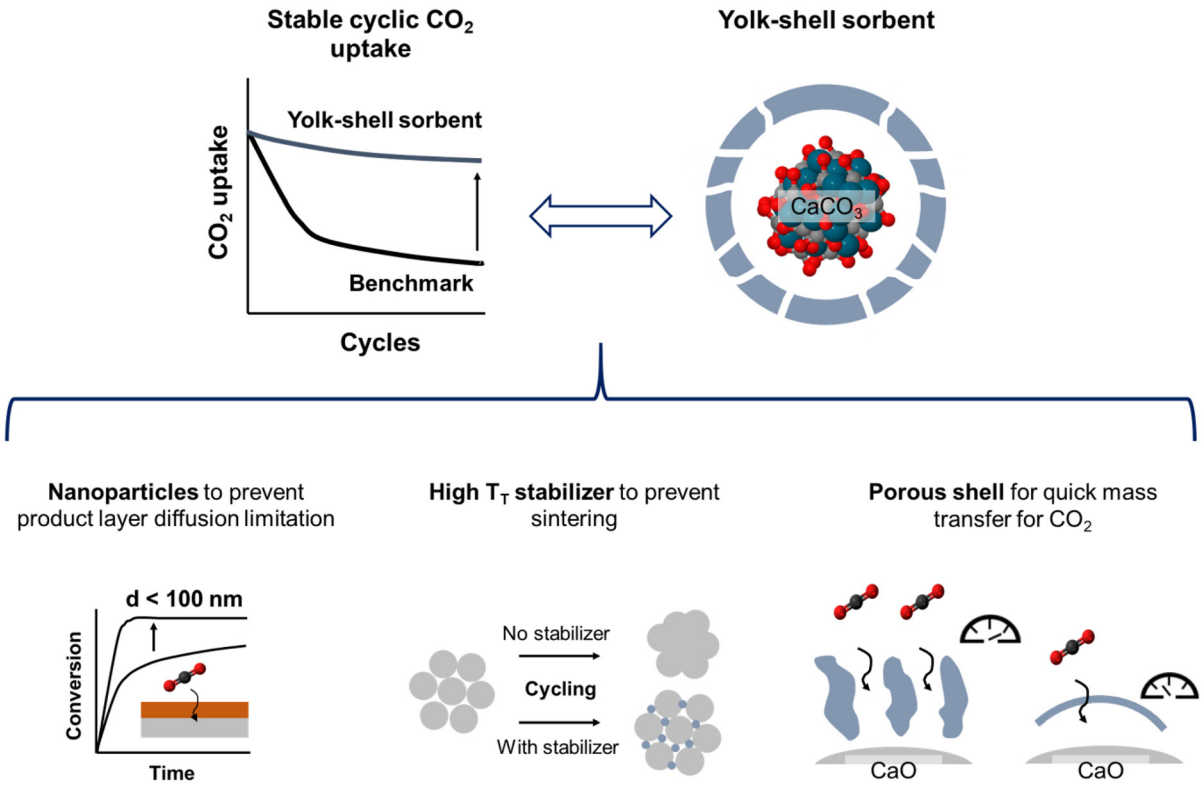


**Fig. 1** Design approach for yolk–shell-type CaO-based sorbents. Using a nanoparticle core is expected to prevent diffusive limitations due to product layer formation, whereas a porous shell of a high $T_T$ stabilizer shall mitigate sintering of the nanoparticles while at the same time allowing for a rapid transfer of $CO_2$ to unreacted CaO.

solution of ammonia (VWR International) was added and the reaction mixture was stirred for 5 hours at room temperature. The coated particles were collected by centrifugation, washed in deionized water, and dried at 60 °C overnight.

**2.1.2 Deposition of a $ZrO_2$-shell.** To deposit a shell of $ZrO_2$ onto the carbonaceous shell-coated $CaCO_3$ nanoparticles the method reported by Arnal *et al.* was used.[45] Here, an aqueous solution of Lutensol AO 5 (BASF) was prepared by mixing 11 g of deionized water with 0.43 g of Lutensol AO 5. The aqueous Lutensol AO 5 solution was ultrasonicated for ~10 minutes to ensure a homogeneous mixture. Subsequently, 50 mg of the carbon-coated $CaCO_3$ nanoparticles were added to a mixture of 100 g of ethanol and 0.5 mL of the aqueous Lutensol AO 5 solution. The obtained suspension was ultrasonicated for 30 minutes to disperse the sorbent particles. The mixture was then stirred for 60 minutes at 350 rpm in order to homogenize the suspension. Subsequently, varying amounts (5–200 μL) of a zirconium(IV) butoxide solution (80 wt% in butanol, Sigma-Aldrich) were diluted in 0.5 mL of ethanol. The diluted zirconium(IV) butoxide solution was slowly added to the suspension under continuous stirring. The reaction proceeded under magnetic stirring in an oil bath at 35 °C for 16 hours. Afterwards, the particles were collected by centrifugation and washed in deionized water and ethanol. The obtained zirconia-coated particles were dried at 60 °C overnight. For the synthesis of core–shell sorbents, the same procedure was directly applied to the $CaCO_3$ nanoparticles without the carbonaceous template coating. To yield the final core–shell and yolk–shell architectures, the sorbents were calcined at 900 °C (heating ramp of 50 °C $min^{-1}$) in synthetic air for 10 min.

## 2.2 Characterization

**2.2.1 Electron microscopy.** A JEOL JEM-1400 Plus transmission electron microscope (TEM) with an operating voltage of 120 kV was used to image the sorbent nanoparticles. The samples were prepared by ultrasonication in ethanol for 15–20 min and subsequently deposited onto a carbon coated Cu grid. To visualize the textural properties of the sorbents, a FEI Talos F200X was used, operating in scanning transmission electron microscopy (STEM) mode at an operating voltage of 200 kV. The instrument was equipped with a high-brightness field-emission gun, a high-angle annular dark-field (HAADF) detector, and a large collection-angle energy-dispersive X-ray (EDX) detector, which was used for the compositional analysis of the samples.

A FEI Magellan 400 FEG high resolution scanning electron microscope (SEM) was used for the textural and morphological analysis of the synthesized sorbents. The instrument was operated at an acceleration voltage of 10 kV and a beam current of 25 pA. To minimize charging effects during imaging, the samples were sputtered with a 4 nm thick film of Pt/Pd (80 : 20) prior to SEM analysis.

**2.2.2 X-ray powder diffraction (XRD).** XRD analysis was carried out on a PANalytical Empyrean diffractometer using Cu $K_\alpha$ radiation with a wavelength of $\lambda \approx 1.5418$ Å in a reflection geometry. In a typical *ex situ* XRD experiment, the measurement was carried out for 65 min from 5–90° at a step size of 0.0167°. In order to quantify the weight fractions of the individual crystal phases, Rietveld refinement was carried out using the FullProf Suite software. More details on the Rietveld method and the refinement data can be found in the ESI.†

**2.2.3 Raman spectroscopy.** Raman spectroscopy was performed on a DXR 2 Raman spectrometer (Thermo Fisher) equipped with a 532 nm excitation laser with a spot size of 2.1 μm. All *ex situ* measurements were performed in air at atmospheric pressure using a laser power in the range 2–5 mW. Four to six measurements at different locations of the sample with a measurement time ranging between 5–20 s were acquired and averaged. For *in situ* Raman measurements, a high-temperature Linkam CCR1000 cell was used. For the carbonaceous template removal, the sample was heated to 600 °C (heating rate of 10 °C $min^{-1}$) under 50 ml $min^{-1}$ of synthetic air. The temperature was held every 25 °C to collect Raman spectra.

**2.2.4 Thermogravimetric analysis (TGA).** Cyclic $CO_2$ capture–release experiments were conducted in a thermogravimetric analyzer (Mettler Toledo TGA/DSC 3+) with a reaction chamber volume of 45 mL. Under harsh regeneration conditions, calcination was performed at 900 °C for 5 min in 80 vol% $CO_2$. The carbonation reaction was performed at 650 °C for 20 minutes in 15 vol% $CO_2$. The heating and cooling ramps between the carbonation and calcination temperatures were set to 50 °C $min^{-1}$ (in $N_2$). Prior to the first carbonation reaction, each sample was calcined at 900 °C in synthetic air for 10 min. The total volumetric gas flow was set to 200 mL $min^{-1}$ throughout the entire experiment. The $CO_2$ uptake, $C_{CO_2,i}$, was determined *via*:

$$C_{CO_2,i} = \frac{m_{carb,i} - m_{calc}}{m_{calc}} \quad (1)$$

where $m_{carb,i}$ is the mass of the sorbent at the end of the carbonation step of cycle number $i$ and $m_{calc}$ is the mass of the calcined sorbent after the first calcination.

# 3. Results and discussion

## 3.1 Synthesis of the yolk–shell sorbents

To yield CaO–$ZrO_2$-based yolk–shell-structured sorbents, a two-step synthesis approach was performed (Fig. 2a). First, commercial $CaCO_3$ nanoparticles (Ca-NP, $d_{avg,CaCO_3}$ = 67 nm, Fig. 2b) were coated with a carbonaceous shell (Ca@C, Fig. 2c).[44] The thickness of the coating was about 40 nm, an optimized value to ensure a homogeneous carbonaceous layer, while avoiding the formation of separate carbonaceous spheres (Fig. S1†). The homogeneity of the carbonaceous coating was confirmed by EDX-TEM (Fig. 2c).

In the second step of the synthesis, the Ca@C particles were coated with a layer of $Zr(OH)_4$ utilizing a wet-chemistry-based approach (see Materials section for details).[45] A homogeneous coating with $Zr(OH)_4$ (see below) was confirmed *via* EDX-TEM, see Fig. 2d. The resulting yolk–shell structure after calcination (synthetic air, 900 °C) is shown in Fig. 2e and will be discussed in more detail further below. Throughout this work, the nomenclature for yolk–shell sorbents will be Ca@*x*Zr, where *x* is the experimentally determined amount of $ZrO_2$ (in wt%) in the sorbent. As a reference material, $CaCO_3$ NPs (Ca-NP) were also directly coated with zirconia using the same coating procedure but without addition of the carbonaceous shell, yielding core–shell sorbents. Throughout the manuscript, the core–shell sorbents will be referred to as Ca–*x*Zr.

The structure of the as-synthesized (*i.e.* before the first calcination) sorbents was assessed by XRD and Raman spectroscopy. The XRD patterns of the reference material and the zirconia-stabilized yolk–shell and core–shell-type sorbents are shown in Fig. 2f. The diffractogram of Ca-NP (as received) showed only the characteristic diffraction peaks of $CaCO_3$ (calcite polymorph). Also all of the yolk–shell and core–shell sorbents showed the diffraction peaks due to $CaCO_3$. An amorphous halo with a maximum around approximately $2\theta = 30°$, relating to amorphous $Zr(OH)_4$, was observed in the sorbents prior to their calcination.[46] The $ZrO_2$ content in the sorbents was estimated using Rietveld analysis of XRD data acquired of sorbents that have undergone 20 cycles and are listed in Table 1 (see Fig. S2 and Table S1† for details on the Rietveld refinement). The Raman spectra of the as-synthesized sorbents are shown in Fig. 2g. All yolk–shell sorbents (prior to calcination) showed features due to the D-band (1350 $cm^{-1}$) and G-band (1574 $cm^{-1}$) of carbon confirming the presence of a carbonaceous coating. These sorbents also show a weak band related to amorphous $Zr(OH)_4$ between 590 and 670 $cm^{-1}$, confirming the Zr phase observed in XRD.[47] Additional features related to $CaCO_3$ (158 $cm^{-1}$, 284 $cm^{-1}$, 713 $cm^{-1}$, 1087 $cm^{-1}$) were observed as well.

## 3.2 Characterization of as-prepared sorbents after template removal

The as-synthesized sorbents were calcined in synthetic air (80 vol% $N_2$, 20 vol% $O_2$, 10 min at 900 °C, heating ramp of 25 °C $min^{-1}$) to remove the carbonaceous template as well as to decompose $CaCO_3$ into CaO, yielding as-prepared yolk–shell sorbents. The normalized weight (solid line) of Ca@C and the temperature ramp recorded during a TGA measurement (synthetic air, 175 ml $min^{-1}$, heating ramp of 25 °C $min^{-1}$) are shown in Fig. 3a. The initial mass loss (I) ($T < 150$ °C) is related to the release of residual solvent (water and ethanol) from the synthesis. The subsequent weight losses (II) and (III) are related to the removal of the carbonaceous template layer, resulting in a total weight loss of 35 wt% at 550 °C.[48,49] At temperatures >600 °C, an additional weight loss (approximately 30% of the initial weight or 78% of the weight after full decomposition) is observed. This weight loss is due to the decomposition of $CaCO_3$ to CaO through the release of $CO_2$ (CaO has a theoretical $CO_2$ uptake capacity of 0.78 $g_{CO_2}$ $g_{Sorbent}^{-1}$).

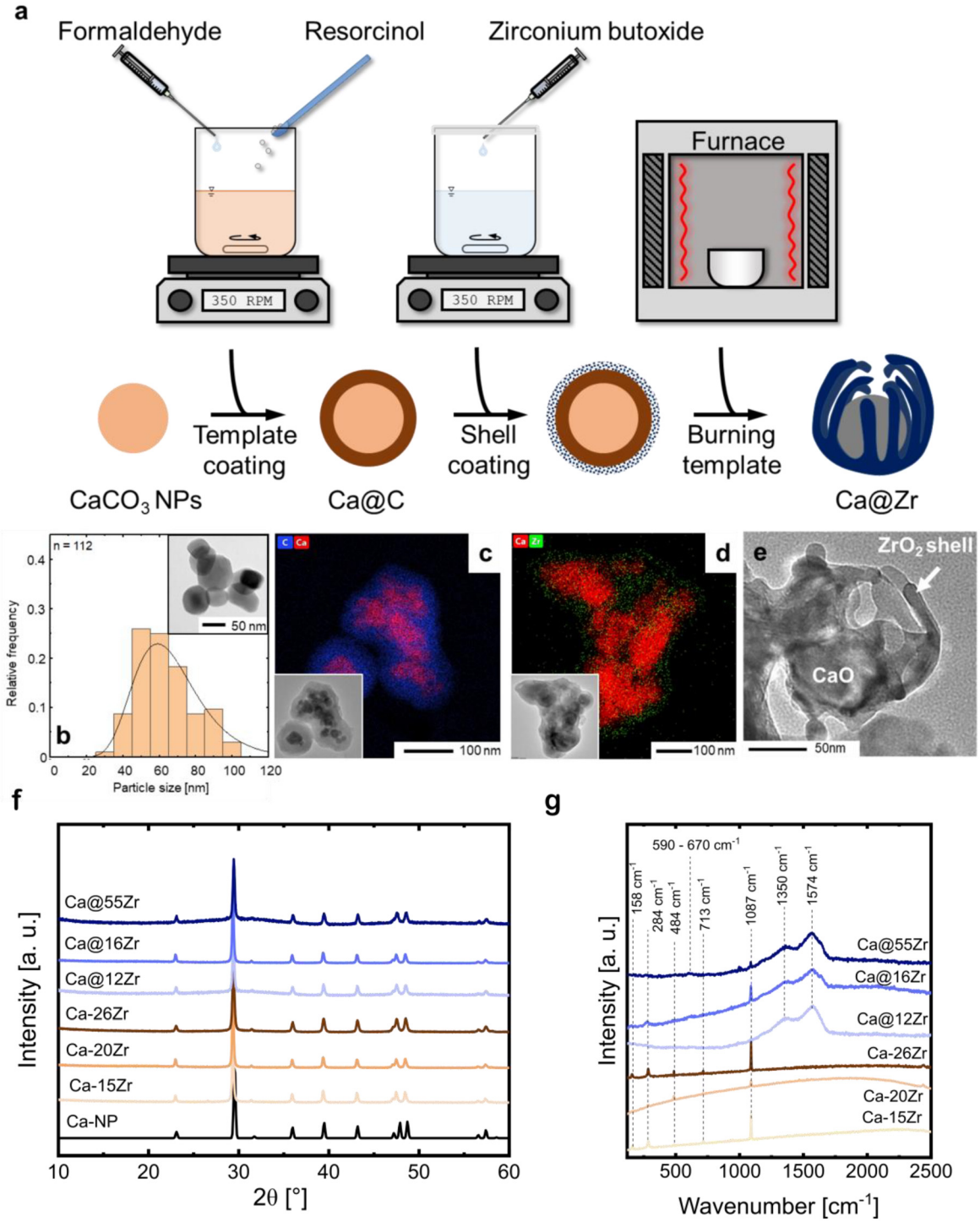


**Fig. 2** (a) Illustration of the two-step synthesis approach to yield yolk–shell-type structures containing a CaO yolk and a $ZrO_2$ shell. (b) Particle size distribution of commercial $CaCO_3$ nanoparticles determined by TEM, (c) TEM micrograph and EDX elemental map of $CaCO_3$ nanoparticles coated with a homogeneous carbonaceous shell with an average thickness of 40 nm, (d) TEM micrograph and EDX elemental map of a sorbent containing both the carbonaceous template coating and the $ZrO_2$ coating, (e) TEM micrograph of the calcined yolk–shell sorbent after template removal in synthetic air at 900 °C, (f) XRD patterns of Ca-NP and as-synthesized (prior to calcination) zirconia-stabilized sorbents, and (g) Raman spectra of as-synthesized sorbents.

To assure that the carbonaceous template was removed completely during calcination in synthetic air, we studied the decomposition and removal of the template by *in situ* Raman spectroscopy. Fig. S3† shows the Raman spectra of Ca@C during heat treatment in synthetic air (up to 550 °C). We observe the disappearance of hydroxyl groups $\nu$(OH), at

 

approximately 2800 $cm^{-1}$, in the temperature range 50 to 100 °C, corresponding to mass release (I) as observed in the TGA measurement. The modes relating to the G-band and D-band of carbon decrease in intensity between 100 and 500 °C. At 550 °C, no features related to the D- and G-band were observed, confirming the complete removal of the carbonaceous template at 550 °C. The characteristic mode for $CO_3^{2-}$ (~1087 $cm^{-1}$) in $CaCO_3$ is present at all temperatures (*i.e.* up to 550 °C). EDX-TEM analysis of the particles before and after calcination confirms the carbon removal; the respective images are shown in Fig. S3b and c.†

**Table 1** $ZrO_2$ content in yolk–shell and core–shell sorbents based on Rietveld analysis (sorbent exposed to 20 carbonation–calcination cycles)

| Type | Sorbent | $ZrO_2$ content [wt%] |
|---|---|---|
| Core–shell | Ca–15Zr | 15 |
| Core–shell | Ca–26Zr | 26 |
| Yolk–shell | Ca@16Zr | 16 |
| Yolk–shell | Ca@12Zr | 12 |
| Yolk–shell | Ca@55Zr | 55 |

The structure of the as-prepared (*i.e.* calcined), zirconia-stabilized sorbents was assessed by XRD (Fig. 3b). The calcined core–shell particles show the characteristic diffraction peaks of both CaO ($Fm\bar{3}m$ space group, cubic) and $CaZrO_3$ (*Pcmn* space group, orthorhombic). Unexpectedly, the intensity of the peaks related to $CaZrO_3$ increased from Ca–15Zr to Ca–26Zr, indicating the formation of larger amounts of the mixed phase with increasing $ZrO_2$ contents. Using Rietveld analysis (see Fig. S2 and Table S1†), we estimated the fraction of the $CaZrO_3$ mixed phase in the core–shell sorbents Ca–15Zr and Ca–26Zr as 15 and 37 wt%, respectively. The XRD patterns of the yolk–shell sorbents Ca@16Zr and Ca@12Zr showed peaks due to CaO

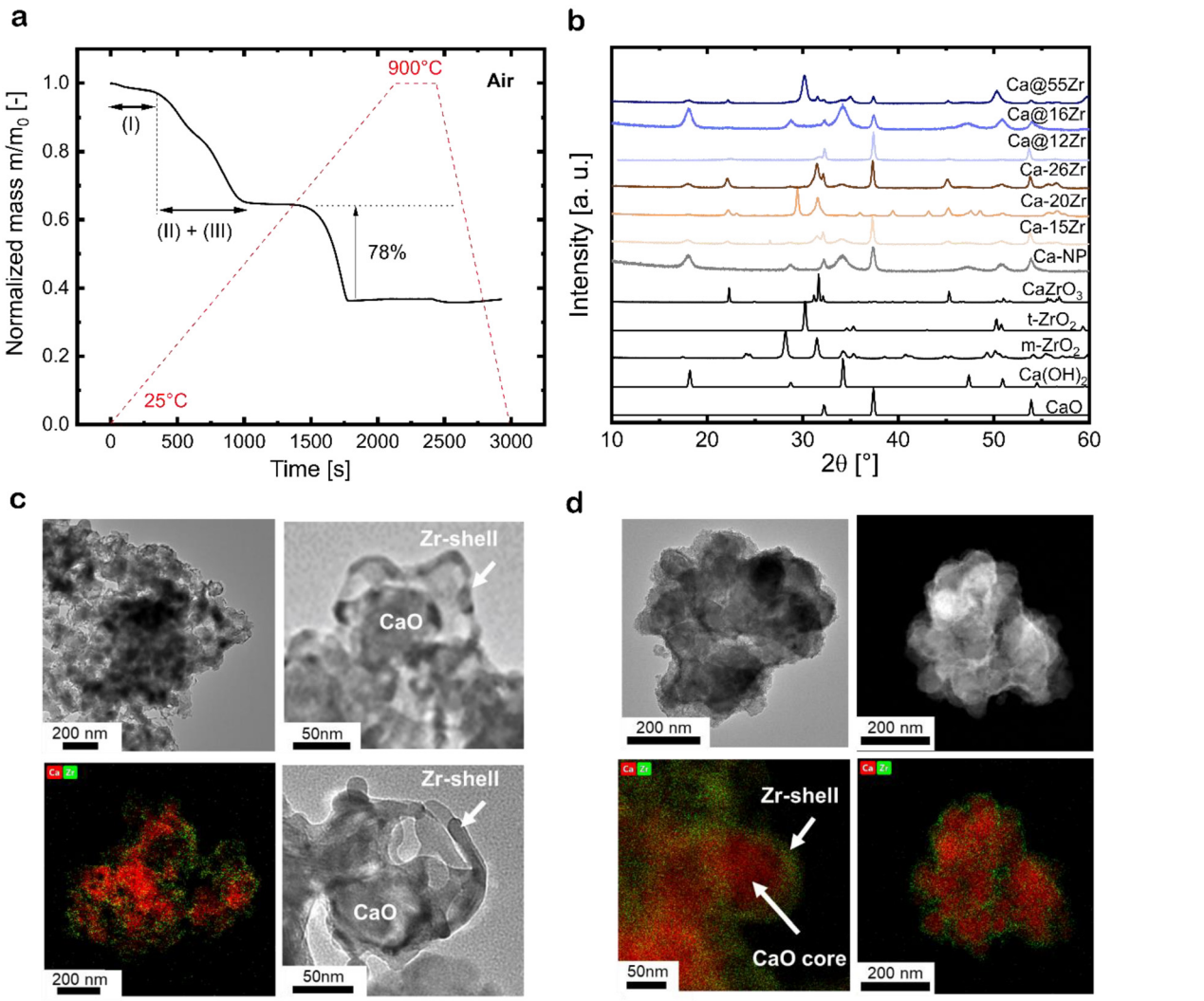


**Fig. 3** (a) Weight loss of $CaCO_3$ nanoparticles containing a carbonaceous template coating during calcination in air (heating ramp of 25 °C $min^{-1}$ up to 900 °C), (b) XRD patterns of calcined zirconia-stabilized sorbents after template removal; TEM micrographs and EDX-TEM elemental maps for Ca and Zr for (c) a zirconia-stabilized, yolk–shell structured sorbent (Ca@12Zr) and (d) a zirconia-stabilized, core–shell-structured sorbent (Ca–26Zr).

and very low intensity peaks possibly due to $CaZrO_3$, which we were not able to quantify using Rietveld refinement (due to their small intensity). This suggests, considering the detection limit of the XRD setup, that in such sorbents the weight fraction of $CaZrO_3$ is <1 wt%. In addition, no peaks due to $ZrO_2$ were observed. Hence, in the yolk–shell sorbents Ca@12Zr and Ca@16Zr Zr is very likely present in an amorphous phase. However, for Ca@55Zr, tetragonal zirconia (t-$ZrO_2$) was observed in addition to both CaO and $CaZrO_3$. Rietveld refinement showed that this sorbent contained about 11 wt% $CaZrO_3$ and 52 wt% t-$ZrO_2$. In conclusion, compared to the core–shell particles, $CaZrO_3$ formation was reduced in the yolk–shell-type sorbents (at similar $ZrO_2$ contents), in particular when comparing Ca@16Zr and Ca–15Zr.

The morphologies of the calcined yolk–shell sorbents and core–shell sorbents were imaged using (EDX-)TEM, see Fig. 3c and d. The yolk–shell-structured sorbents Ca@12Zr (Fig. 3c) and Ca@16Zr (Fig. S4a†) exhibit individual CaO nanoparticles encapsulated by a Zr-containing shell with an occasionally dendritic appearance. The void space between the yolk and the shell, characteristic for the yolk–shell architecture, is clearly visible for Ca@12Zr. Ca@55Zr (Fig. S4b†) showed both larger agglomerates coated with a Zr-containing shell as well as some yolk–shell structures similar to the ones observed for Ca@16Zr and Ca@12Zr. For the larger agglomerates, the distribution of Ca and Zr, based on EDX-TEM, overlapped in intensity, indicating the formation of large $CaZrO_3$ particles or $CaZrO_3$-coated CaO particles, in line with our XRD observations (Fig. 3b). For high Zr contents (Ca@55Zr), TEM also shows the presence of $ZrO_2$ particles, which are, taking into account the XRD results, related to t-$ZrO_2$. The core–shell sorbent Ca–26Zr (Fig. 3d) exhibited a Zr-containing coating covering the whole surface of the CaO particles. Based on our XRD analysis, this coating is composed of a thick layer of $CaZrO_3$. On the other hand, the calcined core–shell sorbent Ca–15Zr (Fig. S4c†) showed an inhomogeneous Zr-containing coating on the CaO particles, indicating that the added amount of $ZrO_2$ was insufficient to completely coat the CaO nanoparticles with a Zr-containing phase. Based on our XRD analysis, we also expect the Zr-containing coating of Ca–15Zr to be $CaZrO_3$.

### 3.3 Cyclic $CO_2$ uptake of the nanostructured zirconia-stabilized sorbents

The cyclic $CO_2$ uptake of the zirconia-stabilized yolk–shell sorbents and the references Ca-NP as well as the core–shell particles were assessed over 20 carbonation–calcination cycles (Fig. 4a). Sorbents with $ZrO_2$ contents <10 wt% were not investigated in more detail because they did not form well-defined yolk–shell structures and hence exhibited a lower $CO_2$ uptake than Ca-NP.

The reference sorbent Ca-NP (without Zr) has a high $CO_2$ uptake of 0.63 $g_{CO_2}$ $g_{Sorbent}^{-1}$ in the first cycle. However, the $CO_2$ uptake decreases rapidly with cycle number, reaching 0.21 $g_{CO_2}$ $g_{Sorbent}^{-1}$ (decrease of 66% compared to the 1st cycle) and 0.17 $g_{CO_2}$ $g_{Sorbent}^{-1}$ (decrease of 73% compared to the 1st cycle) after 10 and 20 cycles, respectively. The $CO_2$ uptake of the yolk–shell-structured sorbents varied substantially with the content of Zr. Compared to Ca-NP (0.17 $g_{CO_2}$ $g_{Sorbent}^{-1}$), Ca@16Zr and Ca@12Zr show significantly higher $CO_2$ uptakes after 20 cycles, reaching, respectively, 0.38 $g_{CO_2}$ $g_{Sorbent}^{-1}$ (maximum theoretical $CO_2$ uptake of 0.65 $g_{CO_2}$ $g_{Sorbent}^{-1}$) and 0.61 $g_{CO_2}$ $g_{Sorbent}^{-1}$ (maximum theoretical $CO_2$ uptake of 0.69 $g_{CO_2}$ $g_{Sorbent}^{-1}$). In particular, the $CO_2$ uptake performance of Ca@12Zr is promising, as it showed a relatively stable $CO_2$ uptake over 20 cycles with only a small decrease from 0.66 $g_{CO_2}$ $g_{Sorbent}^{-1}$ in the 1st cycle to 0.61 $g_{CO_2}$ $g_{Sorbent}^{-1}$ (decrease of 8%) in the 20th cycle. For the sorbent with the highest zirconia content investigated (Ca@55Zr), very low $CO_2$ uptakes of, respectively, 0.17 $g_{CO_2}$ $g_{Sorbent}^{-1}$ and 0.04 $g_{CO_2}$ $g_{Sorbent}^{-1}$ in the 1st and 20th cycle were observed. The low $CO_2$ uptake of Ca-NP@55Zr was due to the large fraction of $CO_2$-capture-inactive t-$ZrO_2$ and $CaZrO_3$ in this material as evidenced by XRD measurements (Fig. 3b). Turning to the core–shell structured sorbents, the most promising core–shell sorbent Ca–26Zr showed a significantly lower $CO_2$ uptake in the 20th cycle (0.29 $g_{CO_2}$ $g_{Sorbent}^{-1}$) compared to Ca@12Zr (0.61 $g_{CO_2}$ $g_{Sorbent}^{-1}$). Further, the core–shell sorbent Ca–15Zr had a $CO_2$ uptake of 0.27 $g_{CO_2}$ $g_{Sorbent}^{-1}$ after 20 cycles, which is significantly lower than the $CO_2$ uptake of its yolk–shell analogue with a similar $ZrO_2$ content, *i.e.* Ca@16Zr (0.38 $g_{CO_2}$ $g_{Sorbent}^{-1}$). Hence, a yolk–shell architecture yielded significantly better performing sorbents compared to the core–shell architecture (and the Ca-NP reference). This observation will be rationalized in the following sections.

### 3.4 The effect of nanostructuring on the carbonation kinetics

The carbonation kinetics in the 1st and 10th cycle of the most promising yolk–shell sorbents (Ca@16Zr and Ca@12Zr) and the core–shell analogues (Ca–15Zr and Ca–26Zr), as well as the reference Ca-NP are plotted in Fig. 4b and c. Independent of the material and the cycle number, the carbonation reaction can be divided into two reaction regimes, *i.e.* a fast, kinetically-controlled regime followed by a slower, diffusion-controlled regime. The effect of the yolk–shell and core–shell architectures on these regimes will be discussed below.

First, we analyzed the effect of the yolk–shell and core–shell architectures on the kinetically-controlled regime. Based on the normalized $CO_2$ uptake rate reaching a plateau, see Fig. 4d, we defined the end of the kinetically-controlled regime at $t$ = 150 s for all sorbents. Within the kinetically-controlled regime in the 1st cycle, the yolk–shell sorbents reached significantly higher $CO_2$ uptakes of 0.56 $g_{CO_2}$ $g_{Sorbent}^{-1}$ (Ca@12Zr) and 0.51 $g_{CO_2}$ $g_{Sorbent}^{-1}$ (Ca@16Zr) compared to the core–shell sorbents (0.3 $g_{CO_2}$ $g_{Sorbent}^{-1}$ for Ca–15Zr and 0.28 $g_{CO_2}$ $g_{Sorbent}^{-1}$ for Ca–26Zr) and Ca-NP (0.35 $g_{CO_2}$ $g_{Sorbent}^{-1}$). Also, the maximum normalized $CO_2$ uptake rate (Fig. 4d) achieved for the yolk–shell sorbents was significantly higher than for Ca–15Zr, Ca–26Zr and Ca-NP. In the 10th cycle, the $CO_2$ uptake at the end of the kinetically-controlled regime was comparable for Ca@12Zr and Ca–26Zr, whereas Ca@16Zr, Ca–15Zr and Ca-NP showed a lower $CO_2$ uptake. The maximum achieved $CO_2$ uptake rate was also slightly higher for the yolk–shell sorbents

 

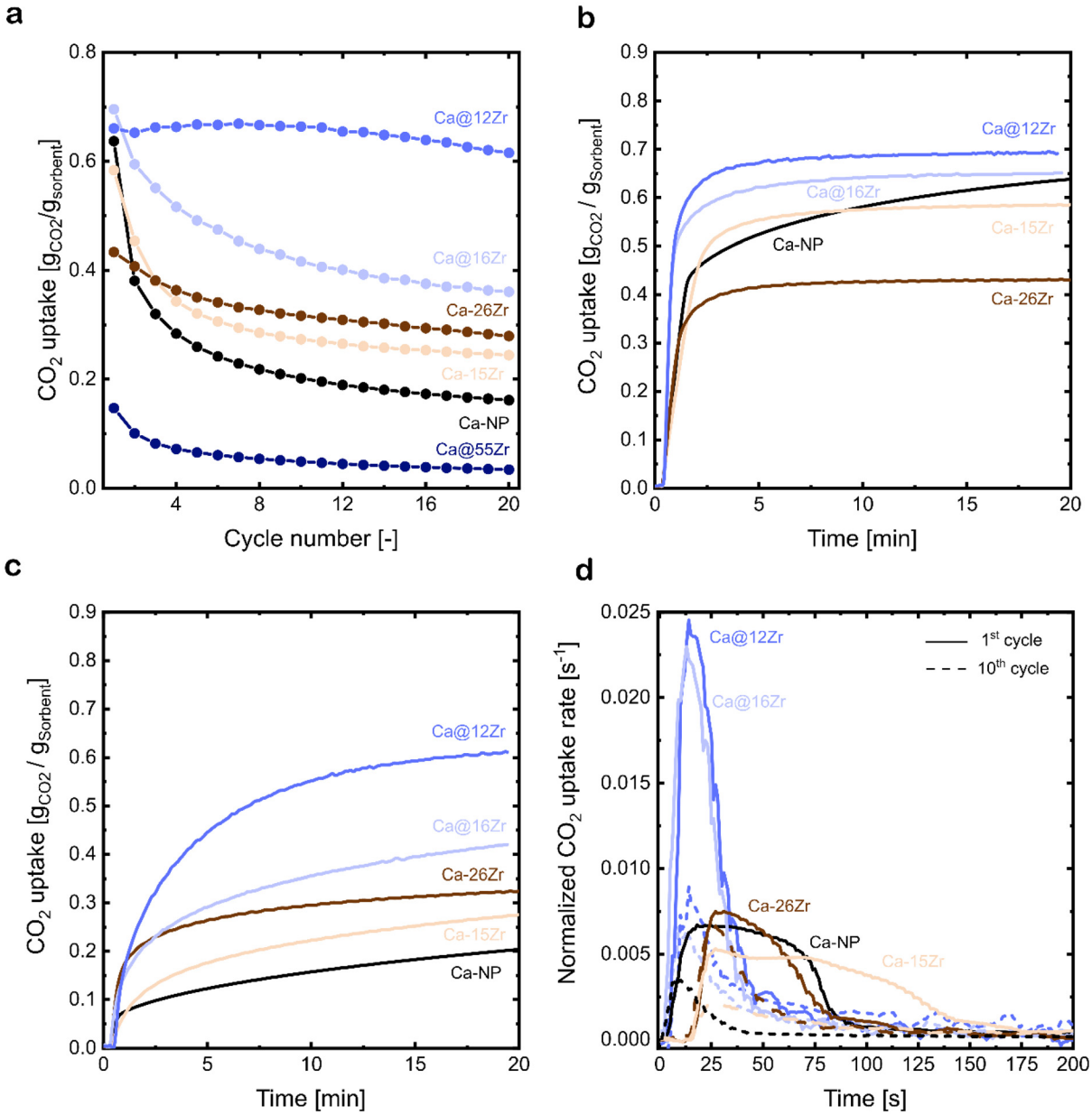


**Fig. 4** (a) Cyclic $CO_2$ uptake over 20 carbonation–calcination cycles of zirconia-stabilized, yolk–shell-structured sorbents as well as core–shell-type sorbents and the $CaCO_3$ NP reference; carbonation at 650 °C in 15 vol% $CO_2$ and calcination at 900 °C in 80 vol% $CO_2$, (b) $CO_2$ uptake as a function of time in the 1st cycle and (c) 10th cycle of zirconia-stabilized sorbents and the $CaCO_3$ NP reference, and (d) normalized $CO_2$ uptake rate during the first 200 s of the 1st (—) and 10th (– – –) carbonation for zirconia-stabilized sorbents and the $CaCO_3$ NP reference.

than for the core–shell sorbents and the Ca-NP reference. In the kinetically-controlled regime in which the $CO_2$ mass transfer resistance to reach the reaction surface is negligible, the reaction proceeds as a surface reaction. Hence, the $CO_2$ uptake rate ($dm_{CO_2}/dt$) is proportional to the reaction surface area $S_0$ and the reaction rate $k_s$:

$$\frac{dm_{CO_2}}{dt} \sim S_0 \cdot k_s \quad (2)$$

As the reaction itself (*i.e.* the carbonation of CaO) has an intrinsic reaction rate $k_s$,[33,50,51] a higher maximum $CO_2$ uptake rate implies a higher reaction surface area of CaO. Hence, we can conclude that a yolk–shell architecture improved the accessibility of CaO for reaction with $CO_2$, *i.e.* provided sorbents with a higher reaction surface area compared to the core–shell sorbents and the Ca-NP reference. $N_2$ physisorption measurements to further confirm this conclusion could not be conducted due to the small amount (<20 mg) of sorbent retained from a single synthesis.

The analysis of the kinetics in the diffusion-controlled regime, *i.e.* $t$ > 150 s, will be discussed next. All sorbents exhibited a comparable $CO_2$ uptake in the diffusion-controlled

regime in the 1st cycle, see Fig. 4b. In the 10th cycle (Fig. 4c), the yolk–shell sorbents achieved a large part of their total $CO_2$ uptake after 20 minutes of carbonation in the diffusion-controlled regime with an average normalized $CO_2$ uptake rate (for 150 s < $t$ < 1200 s) for Ca@12Zr and Ca@16Zr of 2.5 and 1.5 × $10^{-4}$ $s^{-1}$, respectively. The $CO_2$ uptake of the core–shell sorbents in this regime was significantly smaller, reaching an average $CO_2$ uptake rate of 1.04 × $10^{-4}$ $s^{-1}$ and 6.73 × $10^{-5}$ $s^{-1}$ for Ca–15Zr and Ca–26Zr, respectively. The Ca-NP reference exhibited a $CO_2$ uptake rate of 8.0 × $10^{-5}$ $s^{-1}$ and its overall $CO_2$ uptake in the 10th cycle was comparably low. The average $CO_2$ uptake rates in the 20th cycle were consistent with those observed in the 10th cycle and scaled in the following order: Ca@12Zr (2.2 × $10^{-4}$ $s^{-1}$) > Ca@16Zr (1.3 × $10^{-4}$ $s^{-1}$) > Ca–15Zr (9.3 × $10^{-5}$ $s^{-1}$) > Ca–26Zr (7.3 × $10^{-5}$ $s^{-1}$) ≈ Ca-NP (6.7 × $10^{-5}$ $s^{-1}$). Hence, for yolk–shell-structured materials also the $CO_2$ uptake rates in the diffusion-controlled regime were improved compared to the core–shell sorbents and the Ca-NP reference. In particular, the yolk–shell-structured material Ca@16Zr compared favorably with the core–shell sorbent Ca–15Zr which possesses a very similar Zr content. According to the random pore model (RPM), which is widely used to describe the carbonation reaction of CaO, a higher $CO_2$ uptake rate in the diffusion-controlled regime is indicative of a higher effective diffusivity of $CO_2$.[52] Hence, there is a strong indication that the yolk–shell structure improves the effective diffusivity of $CO_2$ compared to core–shell architectures. It is worth noting that the accessibility and availability of CaO for reaction with $CO_2$ may be affected by several factors, including the morphology of the sorbent as well as the structural properties, which will be discussed below.

### 3.5 Stabilization of the morphology during cycling probed by electron microscopy

The analysis of the carbonation kinetics revealed that (i) the maximum $CO_2$ uptake rate in the kinetically-controlled regime is higher for the zirconia-stabilized, yolk–shell-structured sorbents (Ca@12Zr and Ca@16Zr) compared to Ca-NP and the core–shell-structured sorbents, and also (ii) that the $CO_2$ uptake in the diffusion-controlled regime is higher for the yolk–shell-structured sorbents compared to Ca-NP and the core–shell-structured sorbents, implying a higher effective $CO_2$ diffusivity in such materials. In the following, we probe the structural stability of the different sorbent architectures using electron microscopy.

After 10 cycles, the yolk–shell-structured sorbents Ca@12Zr (Fig. 5a) and Ca@16Zr (Fig. S5a†) exhibit Zr-containing shells with a skeletal appearance that encapsulate individual CaO

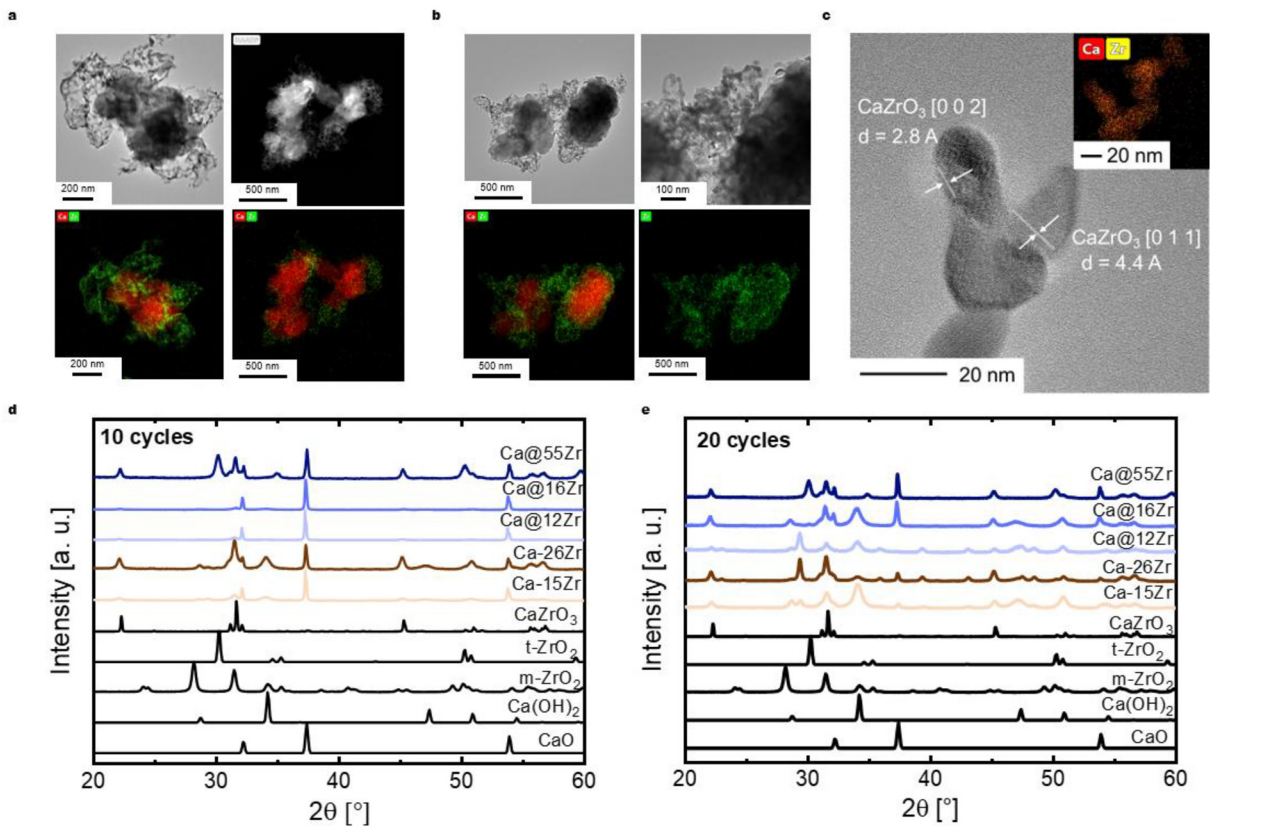


Fig. 5 (a) (EDX-)TEM analysis of the most effective yolk–shell-structured sorbent Ca@12Zr after 10 carbonation–calcination cycles, (b) (EDX-)TEM analysis of the core–shell-structured sorbent Ca–26Zr, (c) high-resolution TEM micrograph and EDX mapping of the dendritic structures observed for all zirconia-stabilized sorbents (here: Ca@16Zr) and XRD patterns of the zirconia-stabilized sorbents after (d) 10 carbonation–calcination cycles as well as (e) 20 carbonation–calcination cycles.

nanoparticles. Compared to the unreacted sorbents, the shells have to some degree lost their shape and integrity, in particular for Ca@16Zr (see Fig. S4a† for comparison). The yolk–shell structure of the as-prepared sorbents is lost to some degree over cycling, resulting in shell structures with higher porosity. Nonetheless, SEM micrographs of Ca@12Zr (Fig. S5b†) confirm that after cycling the sorbent is still composed of individual CaO nanoparticles that are surrounded by a protective shell of dendritic appearance. Based on EDX-TEM analysis, the shells of the yolk–shell sorbents are Zr-containing. After 20 cycles (see Fig. S5d–h†), large agglomerates of yolk–shell particles (in this case Ca@12Zr) are observed. The morphology of the individual particles is therefore difficult to assess. Some of the larger dendritic structures observed for the cycled yolk–shell sorbents consist of smaller crystallites as shown in Fig. 5c. The high-resolution TEM micrograph of these smaller crystallites reveal plane distances that resemble the spacings of the [0 0 2] and [0 1 1] planes of $CaZrO_3$.

On the other hand, electron microscopy-based analysis of the core–shell sorbent Ca–26Zr after 10 cycles shows large CaO agglomerates surrounded by a Zr-containing layer (Fig. 5b). These particles also exhibited Zr-containing dendritic structures covering the surface of the CaO particles. EDX-TEM shows that the Zr coating is in intimate contact with the CaO surface, indicative of the formation of the Ca–Zr mixed phase. In addition, Ca–15Zr (Fig. S5c†) showed enlarged (*i.e.* sintered) CaO particles with dendritic coating structures at the surface. Indeed, cycled Ca–15Zr does not feature a homogeneous coating around CaO particles anymore. To conclude, a yolk–shell-structured architecture protected the single CaO nanoparticles from sintering more effectively than a core–shell-structured morphology. We expect the $ZrO_2$- (or $CaZrO_3$-) shell to act as a physical barrier against sintering between single CaO nanoparticles, reducing in turn sintering,[6,29,53] whereby the yolk–shell architecture seems to be more effective in reducing the interfacial area between the individual CaO nanoparticles. Further, the high porosity of the yolk–shell-structured morphology allowed for a fast transport of $CO_2$ to the surface of the CaO particles. In contrast, for core–shell-type particles the intimate contact between zirconia and CaO led to the formation of a thick Zr-containing shell (likely $CaZrO_3$, see below) that reduced the rate of $CO_2$ uptake by creating diffusional resistance for $CO_2$. The formation of $CaZrO_3$ over cycling will be discussed below.

### 3.6 Delay in $CaZrO_3$ formation during cycling in yolk–shell-structured sorbents

XRD measurements of the as-prepared sorbents showed that the yolk–shell architecture reduces the degree of $CaZrO_3$ formation compared to the core–shell morphologies. In the following we track the formation of $CaZrO_3$ over repeated carbonation–calcination cycling and its correlation with sorbent deactivation.

The XRD patterns of zirconia-stabilized yolk–shell and core–shell sorbents after 10 and 20 cycles are shown in Fig. 5d and e, respectively. Using Rietveld analysis (Table S1†), we estimate the fraction of $CaZrO_3$ in the different materials and define the parameter $\alpha$, *i.e.* the molar ratio of $CaZrO_3$ to the total molar amount of CaO in the as-synthesized sorbent (see Table 2):

$$\alpha = \frac{n_{CaZrO_3}}{n_{CaO}} \quad (3)$$

In the core–shell sorbent Ca–15Zr the ratio $\alpha$ increased slightly from 0.07 (as-prepared) to 0.08 after 20 cycles. This small increase is however within the accuracy of the experiment. Therefore, we conclude that in Ca–15Zr most, if not all, of the $CaZrO_3$ phase already formed after the initial calcination step. For Ca–26Zr, $\alpha$ was 0.21 (as-prepared), 0.20 (10 cycles) and 0.24 (20 cycles). Hence, also for Ca–26Zr most of the Zr is in the form of $CaZrO_3$ after the initial calcination step. The intimate contact between Ca and Zr-containing phases in the core–shell-based architectures leads to the rapid formation of a $CO_2$-capture-inactive $CaZrO_3$ layer around CaO particles (as also evidenced by TEM analysis). Hence, the deactivation of the core–shell sorbents over repeated carbonation–calcination cycles is not driven by the additional formation of $CaZrO_3$. Instead, it is very likely that deactivation is due to the sintering of the individual CaO particles and an increase in the density (and thickness) of the $CaZrO_3$ layer itself (as a result of sintering). This reduces the size of the active surface area and decreases the effective diffusivity of $CO_2$.

The XRD patterns of the yolk–shell sorbents after 10 and 20 cycles (Fig. 5d and e) show the presence of $CaZrO_3$. The values of $\alpha$ after 10 cycles are 0.03 and 0.04 for Ca@16Zr and Ca@12Zr, respectively. Hence, for yolk–shell-structured sorbents the fraction of $CaZrO_3$ increased significantly with cycle number (the as-prepared materials have $\alpha < 0.01$). After 20 cycles, $\alpha$ increased further to 0.09 for Ca@16Zr and 0.07 for Ca@12Zr, indicating a continuing formation of $CaZrO_3$ during cycling. In addition, a small peak due to t-$ZrO_2$ (approximately 1 wt%) was observed for Ca@16Zr (20 cycles). This continuing formation of $CO_2$-capture-inactive $CaZrO_3$ for the yolk–shell-structured materials, in particular for Ca@12Zr, is one explanation for their decreasing $CO_2$ uptake with cycle number (~40% decrease from the 1st to 20th cycle for Ca@16Zr), yet sintering of CaO nanoparticles must also contribute to the decay in the $CO_2$ uptake for Ca@16Zr. For Ca@12Zr on the other hand, the formation of $CaZrO_3$ would result in a theoretical loss of approximately 6 wt% of the initially available CaO. At the same time, Ca@12Zr shows a drop in the cyclic $CO_2$ uptake from the 1st to the 20th cycle of ~8%, *i.e.* for Ca@12Zr

Table 2 Molar ratio of $CaZrO_3$ to CaO derived from Rietveld analysis

| Sorbent | Ratio as-prepared | Ratio after 10 cycles | Ratio after 20 cycles |
|---|---|---|---|
| Ca–15Zr | 0.07 | 0.08 | 0.08 |
| Ca–26Zr | 0.21 | 0.20 | 0.24 |
| Ca@16Zr | <0.01 | 0.03 | 0.09 |
| Ca@12Zr | <0.01 | 0.04 | 0.07 |

the loss of reactive CaO due to $CaZrO_3$ formation accounts to ~75% of the decay in $CO_2$ uptake. Hence, the yolk–shell-structured architecture of Ca@12Zr largely prevented sintering of the CaO nanoparticles, making the loss of reactive CaO through the formation of $CaZrO_3$ the dominating deactivation mechanism. The formation of $CaZrO_3$ is likely a result of the partial loss of the yolk–shell-type structure during cycling, as evidenced in our TEM analysis (Fig. 5a). Hence, the sacrificial template can reduce the amount of $CaZrO_3$ formation during the first cycles, but cannot prevent entirely the contact between CaO and $ZrO_2$.

## 4. Conclusion

In this work, we designed and synthesized yolk(CaO)–shell ($ZrO_2$)-structured sorbents for $CO_2$ capture. The nanostructured materials developed here exceeded the $CO_2$ uptake of the bare CaO nanoparticle benchmark by more than 250% after 20 carbonation–calcination cycles. Comparing the performance of yolk–shell-structured sorbents with that of core–shell structures for which there is an intimate contact between the stabilizer ($ZrO_2$) and CaO, we demonstrate that the yolk–shell-structured materials have a significantly reduced rate of deactivation. The void space between the stabilizer shell and CaO nanoparticle, introduced by a sacrificial carbonaceous template, is crucial to increase the effective diffusivity of $CO_2$, delay the formation of $CaZrO_3$ and stabilize the individual CaO nanoparticles against sintering. The yolk–shell-structured sorbent with a $ZrO_2$ content of 12 wt% performs best and in this material the gradual formation of $CaZrO_3$ with cycle number is the main deactivation mechanism, accounting for 75% of the overall decay in the cyclic $CO_2$ uptake over 20 cycles. Hence, yolk–shell architectures can successfully mitigate sintering, but need to be optimized further to reduce the loss of active CaO. Another important aspect for future work is to develop strategies to maintain the initial yolk–shell-type structure during high-temperature pretreatment and cycling. Furthermore, the use of stabilizers that do not form a mixed phase with CaO under calcium looping conditions, *e.g.* magnesium oxide, may help to provide a yolk–shell architecture with even higher $CO_2$ uptakes and prolonged stability.

## Author contributions

M. K. and C. R. M. conceived and planned the project. M. K. performed the material synthesis, performance characterization, structural characterization as well as SEM analysis. A. O. performed the material synthesis, performance characterization and structural characterization. J. N. performed the material synthesis and structural characterization. A. L. and A. K. performed (EDX-)TEM characterization. M. K. wrote the manuscript with input from all authors. F. D. and A. H. B. revised the manuscript. C. R. M. supervised the project, wrote and revised the manuscript.

## Conflicts of interest

The authors have no conflicts of interest to declare.

## Acknowledgements

This research is based on funding by the European Research Council (ERC) under the European Union's Horizon 2020 research and innovation program under grant agreement number 819573. We also acknowledge Fondation Claude & Giuliana for financial support. A. O. acknowledges funding by the Swiss Exchange Mobility Program (SEMP) of ETH Zürich and RWTH Aachen University. The authors acknowledge the help of the ScopeM team at ETH Zurich for SEM, TEM and EDX analysis.

## References

1 R. K. Pachauri and L. A. Meyer, Climate Change 2014: Synthesis Report. Contribution of Working Groups I, II and III to the Fifth Assessment Report of the Intergovernmental Panel on Climate Change, 2014.
2 NASA, *Local $CO_2$ concentration at Mauna Loa Observatory*, Hawaii, USA, 2020.
3 G. Krinner, *et al.*, Long-term climate change: Projections, commitments and irreversibility. Climate Change 2013 the Physical Science Basis: Working Group I Contribution to the Fifth Assessment Report of the Intergovernmental Panel on Climate Change, 2013, vol. **9781107057**.
4 D. P. Hanak, E. J. Anthony and V. Manovic, A review of developments in pilot-plant testing and modelling of calcium looping process for $CO_2$ capture from power generation systems, *Energy Environ. Sci.*, 2015, **8**, 2199–2249.
5 A. M. Kierzkowska, R. Pacciani and C. R. Müller, CaO-based $CO_2$ sorbents: From fundamentals to the development of new, highly effective materials, *ChemSusChem*, 2013, **6**, 1130–1148.
6 M. T. Dunstan, F. Donat, A. H. Bork, C. P. Grey and C. R. Müller, $CO_2$ Capture at Medium to High Temperature Using Solid Oxide-Based Sorbents: Fundamental Aspects, Mechanistic Insights, and Recent Advances, *Chem. Rev.*, 2021, **121**, 12681–12745.
7 C. H. Yu, C. H. Huang and C. S. Tan, A review of $CO_2$ capture by absorption and adsorption, *Aerosol Air Qual. Res.*, 2012, **12**, 745–769.
8 G. Manzolini, *et al.*, Economic assessment of novel amine based $CO_2$ capture technologies integrated in power plants based on European Benchmarking Task Force methodology, *Appl. Energy*, 2015, **138**, 546–558.
9 I. M. Bernhardsen and H. K. Knuutila, A review of potential amine solvents for $CO_2$ absorption process: Absorption capacity, cyclic capacity and pKa, *Int. J. Greenhouse Gas Control*, 2017, **61**, 27–48.

 

10 C. Luo, *et al.*, Morphological Changes of Pure Micro- and Nano-Sized $CaCO_3$ during a Calcium Looping Cycle for $CO_2$ Capture, *Chem. Eng. Technol.*, 2012, **35**, 547–554.
11 Z. S. Li, N. S. Cai and Y. Y. Huang, Effect of preparation temperature on cyclic $CO_2$ capture and multiple carbonation-calcination cycles for a new Ca-based $CO_2$ sorbent, *Ind. Eng. Chem. Res.*, 2006, **45**, 1911–1917.
12 R. Barker, The reversibility of the reaction $CaCO_3 \rightleftarrows CaO + CO_2$, *J. Appl. Chem. Biotechnol.*, 2007, **23**, 733–742.
13 K. Wang, P. T. Clough, P. Zhao and E. J. Anthony, Synthesis of highly effective stabilized CaO sorbents via a sacrificial N-doped carbon nanosheet template, *J. Mater. Chem. A*, 2019, **7**, 9173–9182.
14 A. Kurlov, *et al.*, Mechanochemically Activated, Calcium Oxide-Based, Magnesium Oxide-Stabilized Carbon Dioxide Sorbents, *ChemSusChem*, 2016, **9**, 2380–2390.
15 S. M. Kim, *et al.*, In Situ XRD and Dynamic Nuclear Polarization Surface Enhanced NMR Spectroscopy Unravel the Deactivation Mechanism of CaO-Based, $Ca_3Al_2O_6$-Stabilized $CO_2$ Sorbents, *Chem. Mater.*, 2018, **30**(4), 1344–1352.
16 C. Chi, Y. Li, W. Zhang and Z. Wang, Synthesis of a hollow microtubular Ca/Al sorbent with high $CO_2$ uptake by hard templating, *Appl. Energy*, 2019, **251**, 113382.
17 Y. Xu, *et al.*, Characteristics and performance of CaO-based high temperature $CO_2$ sorbents derived from a sol-gel process with different supports, *RSC Adv.*, 2016, **6**, 79285–79296.
18 M. Broda and C. R. Müller, Sol-gel-derived, CaO-based, $ZrO_2$-stabilized $CO_2$ sorbents, *Fuel*, 2014, **127**, 94–100.
19 S. M. Kim, A. Armutlulu, A. M. Kierzkowska and C. R. Müller, Inverse Opal-Like, $Ca_3Al_2O_6$-Stabilized, CaO-Based $CO_2$ Sorbent: Stabilization of a Highly Porous Structure To Improve Its Cyclic $CO_2$ Uptake, *ACS Appl. Energy Mater.*, 2019, **2**, 6461–6471.
20 J. Blamey, V. Manovic, E. J. Anthony, D. R. Dugwell and P. S. Fennell, On steam hydration of CaO-based sorbent cycled for $CO_2$ capture, *Fuel*, 2015, **150**, 269–277.
21 M. Krödel, A. Landuyt, P. M. Abdala and C. R. Müller, Mechanistic Understanding of CaO-Based Sorbents for High-Temperature $CO_2$ Capture: Advanced Characterization and Prospects, *ChemSusChem*, 2020, **13**, 6259–6272.
22 A. Kurlov, A. M. Kierzkowska, T. Huthwelker, P. M. Abdala and C. R. Müller, $Na_2CO_3$-modified CaO-based $CO_2$ sorbents: The effects of structure and morphology on $CO_2$ uptake, *Phys. Chem. Chem. Phys.*, 2020, **22**, 24697–24703.
23 Y. Xu, *et al.*, Structure and surface insight into a temperature-sensitive CaO-based $CO_2$ sorbent, *Chem. Eng. J.*, 2022, **435**, 134960.
24 M. Broda, A. M. Kierzkowska and C. R. Müller, Application of the sol-gel technique to develop synthetic calcium-based sorbents with excellent carbon dioxide capture characteristics, *ChemSusChem*, 2012, **5**, 411–418.
25 H. Lu, A. Khan and P. G. Smirniotis, Relationship between structural properties and $CO_2$ capture performance of CaO-based sorbents obtained from different organometallic precursors, *Ind. Eng. Chem. Res.*, 2008, **47**, 6216–6220.
26 M. A. Naeem, *et al.*, Optimization of the structural characteristics of CaO and its effective stabilization yield high-capacity $CO_2$ sorbents, *Nat. Commun.*, 2018, **9**, 1–11.
27 W. Liu, *et al.*, Synthesis of sintering-resistant sorbents for $CO_2$ capture, *Environ. Sci. Technol.*, 2010, **44**, 3093–3097.
28 L. Zhang, Y. Lu and M. Rostam-Abadi, Sintering of calcium oxide (CaO) during $CO_2$ chemisorption: A reactive molecular dynamics study, *Phys. Chem. Chem. Phys.*, 2012, **14**, 16633–16643.
29 K. S. Sultana, D. T. Tran, J. C. Walmsley, M. Rønning and D. Chen, CaO Nanoparticles Coated by $ZrO_2$ Layers for Enhanced $CO_2$ Capture Stability, *Ind. Eng. Chem. Res.*, 2015, **54**, 8929–8939.
30 M. Zhao, *et al.*, Durability of CaO-$CaZrO_3$ sorbents for high-temperature $CO_2$ capture prepared by a wet chemical method, *Energy Fuels*, 2014, **28**, 1275–1283.
31 J. Cai, S. Wang and C. Kuang, ScienceDirect A Modified Random Pore Model for Carbonation Reaction of CaO-based limestone with $CO_2$ in Different Calcination-carbonation Cycles, *Energy Procedia*, 2017, **105**, 1924–1931.
32 A. Di Giuliano, K. Gallucci and P. U. Foscolo, Determination of Kinetic and Diffusion Parameters Needed to Predict the Behavior of CaO-Based $CO_2$ Sorbent and Sorbent-Catalyst Materials, *Ind. Eng. Chem. Res.*, 2020, **59**, 6840–6854.
33 Y. Li, Z. Li, H. Wang and N. Cai, CaO carbonation kinetics determined using micro-fluidized bed thermogravimetric analysis, *Fuel*, 2020, **264**, 116823.
34 H. Sun, *et al.*, Fundamental studies of carbon capture using CaO-based materials, *J. Mater. Chem. A*, 2019, **7**, 9977–9987.
35 D. Alvarez and J. C. Abanades, Pore-size and shape effects on the recarbonation performance of calcium oxide submitted to repeated calcination/recarbonation cycles, *Energy Fuels*, 2005, **19**, 270–278.
36 S. K. Bhatia and D. D. Perlmutter, Effect of the product layer on the kinetics of the $CO_2$–lime reaction, *AIChE J.*, 1983, **29**, 79–86.
37 Z. S. Li, F. Fang, X. Y. Tang and N. S. Cai, Effect of temperature on the carbonation reaction of CaO with $CO_2$, *Energy Fuels*, 2012, **26**, 2473–2482.
38 G. Grasa, R. Murillo, M. Alonso and J. C. Abanades, Application of the random pore model to the carbonation cyclic reaction, *AIChE J.*, 2009, **55**(5), 1246–1255.
39 D. Alvarez and J. Carlos Abanades, Determination of the critical product layer thickness in the reaction of CaO with $CO_2$, *Ind. Eng. Chem. Res.*, 2005, **44**, 5608–5615.
40 N. Mahinpey, M. H. Sedghkerdar, A. Aqsha and A. H. Soleimanisalim, $CO_2$ Capture Performance of Core/Shell CaO-Based Sorbent Using Mesostructured Silica and Titania in a Multicycle $CO_2$ Capture Process, *Ind. Eng. Chem. Res.*, 2016, **55**, 4532–4538.
41 W. Peng, Z. Xu, C. Luo and H. Zhao, Tailor-Made Core-Shell $CaO/TiO_2$-$Al_2O_3$ Architecture as a High-Capacity and

Long-Life $CO_2$ Sorbent, *Environ. Sci. Technol.*, 2015, **49**, 8237–8245.

42 S. Zhang and X. Li, Synthesis and characterization of $CaCO_3$@$SiO_2$ core-shell nanoparticles, *Powder Technol.*, 2004, **141**, 75–79.

43 C. Huang, M. Xu, X. Huai and Z. Liu, Template-Free Synthesis of Hollow $CaO/Ca_2SiO_4$ Nanoparticle as a Cyclically Stable High-Capacity $CO_2$ Sorbent, *ACS Sustainable Chem. Eng.*, 2021, **9**, 2171–2179.

44 X. Fang, *et al.*, Precisely controlled resorcinol–formaldehyde resin coating for fabricating core–shell, hollow, and yolk–shell carbon nanostructures, *Nanoscale*, 2013, **5**, 6908–6916.

45 P. M. Arnal, C. Weidenthaler and F. Schüth, Highly monodisperse zirconia-coated silica spheres and zirconia/silica hollow spheres with remarkable textural properties, *Chem. Mater.*, 2006, **18**, 2733–2739.

46 X. Zhang, *et al.*, Methane decomposition and carbon deposition over $Ni/ZrO_2$ catalysts: Comparison of amorphous, tetragonal, and monoclinic zirconia phase, *Int. J. Hydrogen Energy*, 2019, **44**, 17887–17899.

47 D. S. S. Padovini, D. S. L. Pontes, C. J. Dalmaschio, F. M. Pontes and E. Longo, Facile synthesis and characterization of $ZrO_2$ nanoparticles prepared by the AOP/hydrothermal route, *RSC Adv.*, 2014, **4**, 38484–38490.

48 C. Dwivedi, *et al.*, Resorcinol-formaldehyde coated XAD resin beads for removal of cesium ions from radioactive waste: Synthesis, sorption and kinetic studies, *RSC Adv.*, 2012, **2**, 5557–5564.

49 D. F. Molina-Campos, R. A. Fonseca-Correa, D. P. Vargas-Delgadillo, L. Giraldo and J. C. Moreno-Piraján, Data for the synthesis of resorcinol–formaldehyde aerogels in acidic and basic media, *Data Brief*, 2017, **12**, 409–417.

50 Z. Zhou, P. Xu, M. Xie, Z. Cheng and W. Yuan, Modeling of the carbonation kinetics of a synthetic CaO-based sorbent, *Chem. Eng. Sci.*, 2013, **95**, 283–290.

51 H. Wang, Z. Li, Y. Li and N. Cai, Reduced-order model for CaO carbonation kinetics measured using micro-fluidized bed thermogravimetric analysis, *Chem. Eng. Sci.*, 2021, **229**, 116039.

52 R. H. Borgwardt, K. R. Bruce and J. Blake, An Investigation of Product-Layer Diffusivity for CaO Sulfation, *Ind. Eng. Chem. Res.*, 1987, **26**(10), 1993–1998.

53 P. Sun, J. R. Grace, C. J. Lim and E. J. Anthony, The effect of CaO sintering on cyclic $CO_2$ capture in energy systems, *AIChE J.*, 2007, **53**, 2432–2442.